HOKKAIDO UNIVERSITY

Title	Decadal Response of the Kuroshio Extension Jet to Rossby Waves: Observation and Thin-Jet Theory
Author(s)	Sasaki, Yoshi N.; Minobe, Shoshiro; Schneider, Niklas
Citation	Journal of Physical Oceanography, 43(2), 442-456 https://doi.org/10.1175/JPO-D-12-096.1
Issue Date	2013-02
Doc URL	https://hdl.handle.net/2115/52934
Rights	© Copyright Feb.2013 American Meteorological Society (AMS). Permission to use figures, tables, and brief excerpts from this work in scientific and educational works is hereby granted provided that the source is acknowledged. Any use of material in this work that is determined to be "fair use" under Section 107 of the U.S. Copyright Act or that satisfies the conditions specified in Section 108 of the U.S. Copyright Act (17 USC §108, as revised by P.L. 94-553) does not require the AMS's permission. Republication, systematic reproduction, posting in electronic form, such as on a web site or in a searchable database, or other uses of this material, except as exempted by the above statement, requires written permission or a license from the AMS. Additional details are provided in the AMS Copyright Policy, available on the AMS Web site located at (http://www.ametsoc.org/) or from the AMS at 617-227-2425 or copyright@ametsoc.org.
Type	journal article
File Information	jpo-d-12-096.1.pdf

Hokkaido University Collection of Scholarly and Academic Papers : HUSCAP

Decadal Response of the Kuroshio Extension Jet to Rossby Waves: Observation and Thin-Jet Theory*

YOSHI N. SASAKI AND SHOSHIRO MINOBE

Graduate School of Science, Hokkaido University, Sapporo, Japan

NIKLAS SCHNEIDER

IPRC, and Department of Oceanography, University of Hawaii at Manoa, Honolulu, Hawaii

(Manuscript received 30 May 2012, in final form 9 October 2012)

ABSTRACT

This study examines interannual to decadal variability of the Kuroshio Extension (KE) jet using satellite altimeter observations from 1993 to 2010. The leading empirical orthogonal function (EOF) mode of sea level variability in the KE region represents the meridional shift of the KE jet, followed by its strength changes with a few month lag. This shift of the KE jet lags atmospheric fluctuations over the eastern North Pacific by about three years. Broad sea level anomalies (SLAs) emerge in the eastern North Pacific 3–4 years before the upstream KE jet shift, and propagate westward along the KE jet axis. In the course of the propagation, the meridional scale of the SLAs gradually narrows, and their amplitude increases. This westward propagation of SLAs with a speed of about 5 cm s^{-1} is attributed to the westward propagation of the meridional shift of the jet, consistent with the thin-jet theory, whose importance has been suggested by previous numerical studies. In addition, the westward-propagating signals tend to conserve their quasigeostrophic potential vorticity anomaly, which may explain the characteristic changes of SLAs during the propagation. After the westward-propagating signals of positive (negative) SLAs reach at the east coast of Japan, the upstream KE jet strengthens (weakens) associated with the strength changes of the northern and southern recirculation gyres. Interestingly, this strength change of the KE jet propagates eastward with a speed of about 6 cm s^{-1}, suggesting an importance of advection by the current.

1. Introduction

The Kuroshio Extension (KE) jet, the western boundary current of the subtropical gyre in the North Pacific, transports warm water poleward and yields large heat release from the ocean to the atmosphere. The KE jet exhibits large fluctuations on interannual and decadal time scales (e.g., Deser et al. 1999; Schneider et al. 2002; Qiu and Chen 2005), so its variability has attracted much attention owing to its significant roles not only in the interior ocean structure of the North Pacific (e.g., Qiu and Chen 2011; Oka et al. 2011; Sugimoto and Hanawa 2011) and in marine ecosystem (e.g., Yatsu et al. 2005; Itoh et al. 2009; Nishikawa and Yasuda 2008, 2011) but also in the climate over the North Pacific and North America (e.g., Latif and Barnett 1994; Liu and Wu 2004; Taguchi et al. 2009; Tokinaga et al. 2009; Bond et al. 2010; Kelly et al. 2010; Kwon et al. 2010; Frankignoul et al. 2011). Low-frequency KE variability is also important for decadal prediction because of its long predictability (Mochizuki et al. 2010). One of the prominent features of low-frequency variability in the KE region is the meridional shift of the KE jet, which is captured as a leading empirical orthogonal function (EOF) mode of subsurface temperature variations in the KE region (Taguchi et al. 2007). For example, a large southward shift of the KE jet with an amplitude of 1.5° occurred in the early 1980s (Deser et al. 1999; Joyce and Dunworth-Baker 2003; Nonaka et al. 2006; Sasaki and Schneider 2011a) associated with the climate regime shift in 1976/77 (Nitta and Yamada 1989; Trenberth 1990). Prominent

* International Pacific Research Center Publication Number 924 and School of Ocean and Earth Science and Technology Publication Number 8773.

Corresponding author address: Yoshi N. Sasaki, Science 8th Bldg., 8-3-20, Graduate School of Science, Hokkaido University, N10, W8, Sapporo, 060-0810, Japan.
E-mail: sasakiyo@mail.sci.hokudai.ac.jp

DOI: 10.1175/JPO-D-12-096.1

© 2013 American Meteorological Society

decadal variability in the latitude of the KE jet has been also reported during the period of satellite altimeter observations (e.g., Minobe 2002; Qiu 2003). Interestingly, satellite altimeter observations also suggest that the latitude changes of the KE jet on decadal time scales are roughly coincident with its strength changes (Qiu and Chen 2005, 2010). Similar coherent variability between the latitude and strength of the jet has been seen in idealized numerical model simulations (e.g., Berloff et al. 2007; Pierini et al. 2009).

Nevertheless, the mechanism for the meridional shift of the KE jet and its possible relation to the strength change are not fully understood. It is well established that decadal variability in the KE is largely attributed by westward propagating signals from the central and eastern North Pacific (e.g., Schneider and Miller 2001; Lysne and Deser 2002; Qiu 2003; Kwon and Deser 2007; Ceballos et al. 2009; Sasaki and Schneider 2011a), while westward propagating signals play a lesser role in variability in the Kuroshio–Oyashio confluence region (Qiu 2003; Sugimoto and Hanawa 2011). However, the propagation process and the corresponding response of the KE jet are still under debate. In particular, one puzzling aspect is that wind forcing and the corresponding response of sea level in the eastern North Pacific have a broad spatial scale, but the response in the KE region to the forcing has a much narrower meridional scale (Taguchi et al. 2005, 2007). Taguchi et al. (2007) showed using an eddy-resolving ocean general circulation model (OGCM) output that the traditional linear long Rossby wave in a background state of no flow (e.g., Anderson and Killworth 1979; Gill 1982) can explain the timing of decadal variability of the KE jet, but cannot explain the narrow meridional structure. They hypothesized that the incoming large-scale linear long Rossby waves trigger a narrow-scale intrinsic mode of the KE jet. Nakano and Ishikawa (2010) suggested from an idealized model simulation that the linear long Rossby waves cannot enter the KE region but can induce a southward shift of the KE jet by altering baroclinic instability in the KE region. These studies suggested the importance of linear long Rossby waves.

On the other hand, Sasaki and Schneider (2011a) described variability of the intense KE jet as the temporal evolution of a sharp, nonlinear potential vorticity (PV) front and revealed from an eddy-resolving OGCM output that the meridional shifts of the KE jet result from westward propagating signals along the jet axis with a phase speed comparable to traditional, linear, long Rossby waves. Similar westward propagation of the jet shifts has been also reported in the Gulf Stream region (Sasaki and Schneider 2011b). On the basis of the thin-jet theory by Cushman-Roisin et al. (1993), Sasaki and Schneider (2011a) theoretically explained these westward propagating signals as long Rossby waves along the sharp PV front of the jet. PV anomalies result from meridional shifts of the jet, in contrast to the traditional linear Rossby waves, are trapped along the PV front. Thus, propagating signals in the thin-jet framework occur only on the jet and have a narrow meridional scale.

The purpose of this study is to clarify the mechanism of the westward propagation and to distinguish Rossby waves along the jet in the thin-jet framework, referred to as jet-trapped Rossby waves, from the traditional, linear Rossby waves, referred to as large-scale Rossby waves. To this end, the propagating pathway and spatial structure of westward propagating signals and the corresponding response of the KE jet are examined using satellite altimeter data to observationally test our earlier theoretical and numerical results (Sasaki and Schneider 2011a). The key differences between the jet-trapped and large-scale Rossby waves in the traditional 1.5-layer ocean framework are that the jet-trapped Rossby waves propagate westward along a jet axis with a narrow meridional structure, and their amplitude of sea level anomalies (SLAs) depends on the strength of a jet (Sasaki and Schneider 2011a), but the propagation path of the large-scale Rossby waves is along a constant latitude and their amplitude and meridional scale are independent of a background state (i.e., the KE jet in this case). Also, we document that a shift of the KE jet latitude leads changes of its intensity by a few months and investigate possible underlying mechanisms. In section 2, we describe observations and methods used for describing decadal variability of the KE jet. We identify dominant variability of the KE jet and examine the relation of the meridional shift of the jet to its strength changes in section 3. A spatial structure and pathway of propagating signals and their relation to the position and strength of the KE jet are investigated in section 4. Section 5 and 6 provide discussion and conclusions, respectively.

2. Data and methods

a. Datasets

We use monthly absolute dynamic height and meridional and zonal surface geostrophic velocity data provided by Archiving, Validation, and Interpretation of Satellite Oceanographic data (AVISO) from satellite altimetry combined observations from the Ocean Topography Experiment (TOPEX)/Poseidon, *ERS-1/2*, *Jason-1*, and *Envisat* from January 1993 to December 2010 on a $\frac{1}{3}° \times \frac{1}{3}°$ Mercator grid (Ducet and Le Traon

2001). This dataset employs the mean dynamic topography by Rio and Hernandez (2004). Use of the mean sea surface height by Maximenko et al. (2009) as the climatology yields similar results. We also employ monthly zonal and meridional wind stress at the surface and 1000-hPa geopotential height (Z_{1000}) data from the National Centers for Environmental Prediction–National Center for Atmospheric Research reanalysis (Kalnay et al. 1996). To focus on interannual to decadal variability, a 9-month running mean filter is applied to all monthly data, unless noted otherwise. Similar results can be obtained, even if an 11-month or a 13-month running mean filter is used.

b. Methods

Dominant sea level variability in the KE region is identified by an EOF analysis for SLAs in the KE region (30°–40°N, 140°–170°E). Furthermore, the statistical significance of a correlation coefficient is estimated by a Monte Carlo test using 10 000 random time series that are made by a phase randomization technique (Kaplan and Glass 1995). To determine a lead–lag relation of sea level variability in the KE region to atmospheric fluctuations, we use a singular value decomposition (SVD) analysis, which extracts maximum covariability based on a covariance matrix constructed from two data fields (Bretherton et al. 1992). The SVD analysis is performed between annual mean SLAs in the KE region and wintertime (November–March) Z_{1000} over the North Pacific (10°–90°N, 100°E–60°W) for all combinations of temporally shifted atmospheric fields and with weights proportional to the area represented by grids. The strength of the relation between SLAs and Z_{1000} is measured using three variables: the squared covariance (SC), which is the square of the covariance captured by a SVD mode and is maximized in the SVD analysis; the squared covariance fraction (SCF), which the ratio of SC explained by a SVD mode to the total SC; and the correlation coefficient r between the two time series of a SVD mode.

For analysis of variations of the KE jet, we determine its latitude at each longitude. In the KE region, sea surface height variability is skewed due to shifts of the KE jet (Thompson and Demirov 2006; Sura and Gille 2010). The latitudes of the KE jet axis are generally defined by a position of a fixed contour of sea surface height or subsurface temperature (e.g., Qiu and Chen 2005; Frankignoul et al. 2011) or a position of maximum velocity (e.g., Taguchi et al. 2007; Kelly et al. 2010). However, the former method often misses the intense jet position, especially in the downstream KE region, because the intense KE jet does not always correspond to the same isopleth of sea surface height. In addition, in this method the latitude of the jet is significantly influenced by steric height changes, which have generally broad spatial scale and have less influence on the KE jet position. On the other hand, the latter method may confuse an eddy with a jet, while the effect of steric height changes is quite small. To solve these problems, we propose to combine these two methods. First, we identify a position of a fixed continuous contour of sea surface height from the western boundary (i.e., the east coast of Japan) to the date line in the range from 60 to 120 cm at 10-cm intervals (see Fig. 1a), where the eastern extent (i.e., date line) is determined by the drop of the jet intensity (see Fig. 1b). The influence of an eddy, which has a closed contour, can be removed by this process. Next, at each longitude, the latitude of the maximum absolute velocity is detected over the region where the fixed contours pass. We define this maximum absolute velocity and its position as the strength and the latitude of the KE jet, respectively. In this method we can reduce the influence by steric height changes and mesoscale eddies and can capture the position of the intense jet.

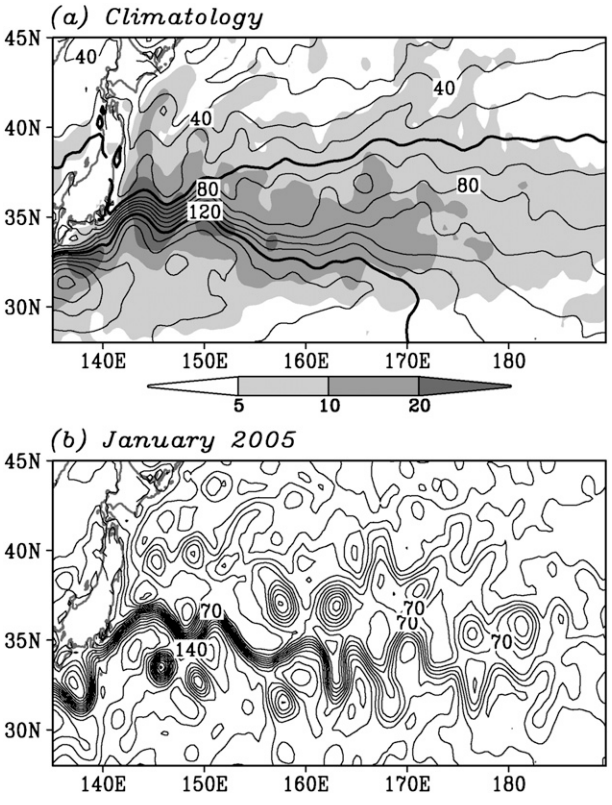

FIG. 1. (a) Climatology (contour) and standard deviations (shading) of sea surface height of the satellite observation: contour interval 10 cm with the thick contour for 60 and 120 cm. The standard deviation is calculated using the data smoothed by a 9-month running mean filter. (b) Monthly mean sea surface height in January 2005: contour interval 10 cm.

3. Dominant Kuroshio Extension variability

Before examining low-frequency variability in the KE region, we briefly summarize major features of the KE jet (Fig. 1). The climatological KE jet penetrates eastward as a free jet after separating from the coast of Japan at 35°N and maintains its sharp frontal structure to 165°E with a meridional scale of 200 km (Fig. 1a). The jet is located along 35°N west of 153°E with a steady meander (Mizuno and White 1983). East of the 153°E, the KE jet shifts southward by about 2° from 35°N to 33°N. The same southward shift is seen in the standard deviation of the low-pass filtered SLAs (shading in Fig. 1a). Farther downstream the climatological sea surface height indicates a broad KE jet, while in monthly mean fields the intense jet with a meridional width of about 100 km extends to the date line (Fig. 1b). This means that the broad climatological jet results from meridional shifts of the intense jet. In monthly mean fields, the surface velocity of the KE jet reaches about 1 m s^{-1} in the upstream region, and is still about 0.5 m s^{-1} around the date line.

Dominant variability of SLAs in the KE region is identified by the EOF analysis. The first EOF mode explains 26.8% of the total sea level variance in the KE region (Fig. 2), twice the explained variance by the second mode (13.4%). Thus, we only focus on this first EOF mode. The corresponding principal component (hereafter PC1) exhibits prominent decadal variability (Fig. 2b). Starting from a negative phase in the mid-1990s, PC1 gradually increases to a positive phase in the early 2000s. PC1 rapidly changes to a negative phase around the mid-2000s and to positive phase in the late 2000s. PC1 reaches maximum values during the end of the analysis period. A seasonal cycle mainly due to the steric height change is superimposed on the decadal fluctuations, while the amplitude of the seasonal changes is much smaller than that of decadal components.

The regression coefficients of SLAs onto PC1 show zonally elongated and meridionally narrow anomalies (Fig. 2a). The large positive SLAs extend from 140° to 165°E, but their meridional scale is only about 200 km. These positive SLAs have two peaks (>20 cm) west of 153°E, which correspond to the ridges of the steady meander of the jet (Fig. 1a). The large negative SLAs located at 37°N, 147°E north of the large positive SLAs are likely related to the changes of the northern recirculation gyre (Jayne et al. 2009), although the areal extent of the negative SLAs is small, probably because the signature of the northern recirculation gyre at the surface is weaker than that at subsurface depths (e.g., Nakano et al. 2008; Jayne et al. 2009). East of 153°E the amplitude of the positive SLAs decreases to less than

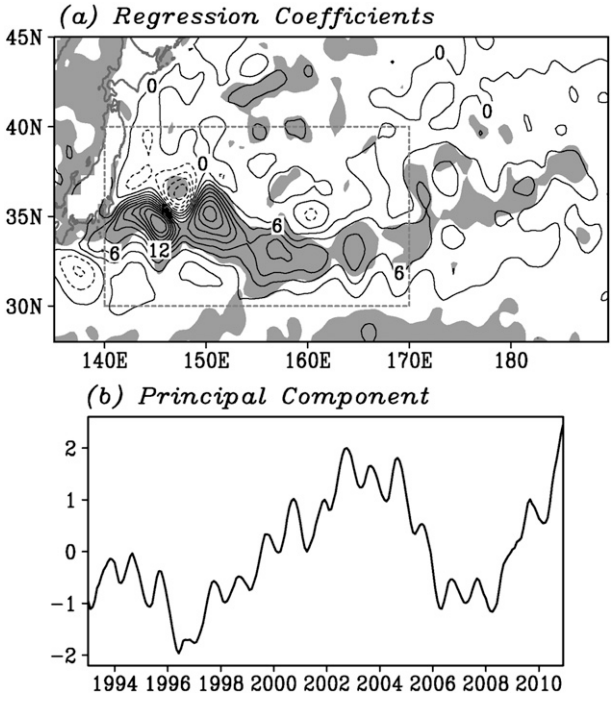

FIG. 2. First EOF mode of monthly SLAs of the satellite observation from 1993 to 2010: total explained sea level variance is 26.8%. (top) Domain of the EOF analysis is denoted by the gray dashed box. The SLA data are smoothed by a 9-month running mean filter. (a) Regression coefficients of SLAs onto the principal component of the first EOF mode: contour interval 3 cm; shading indicates regions where the corresponding correlations are significant at the 95% confidence level. (b) Normalized principal component (PC1).

10 cm, but they still keep the meridionally narrow structure. The location of these positive SLAs shifts southward at 153°E from 35° to 33°N, parallel to the climatological jet position and the large standard deviation of the low-pass filtered SLAs (Fig. 1a). This colocation of the KE jet and the large SLAs is consistent with Taguchi et al. (2007) and will be further investigated in the next section.

To further explore the relation of this leading EOF mode to the changes of the KE jet, we calculate the spatial pattern of the sea surface height corresponding to the positive and negative phases of the first EOF mode (Fig. 3). In the positive phase of the first EOF mode, the KE jet west and east of 153°E is located around 35.5° and 34°N, respectively (Fig. 3a). On the other hand, the upstream KE jet in the negative phase is shifted to the south about 1° compared to the location in the positive phase (Fig. 3b). This latitudinal change of the jet is consistent with the large SLAs being concentrated over the KE jet axis, especially during the negative phase (shading in Fig. 3b). In addition to the shift in latitude, the KE jet is stronger in the positive phase than

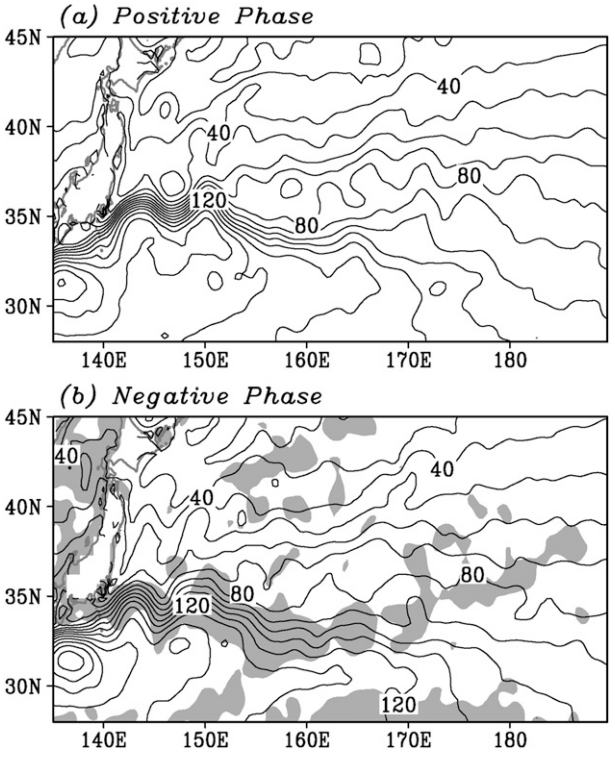

FIG. 3. Sea surface height defined as the climatology (a) plus and (b) minus the regression coefficients of SLAs onto PC1: contour interval 10 cm; shading (lower panel) indicates the regions where the corresponding correlations are significant at the 95% confidence level.

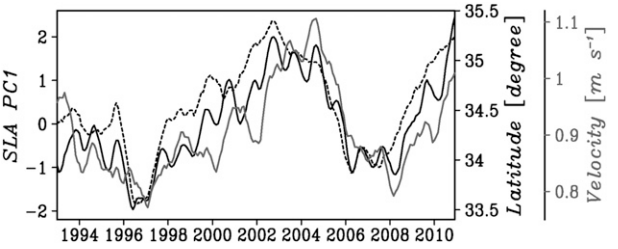

FIG. 4. The latitude (black dotted line) and strength (gray solid line) of the KE jet at the surface averaged over 140°–165°E along with PC1 shown in Fig. 2b (black solid line). The time series of the latitude and velocity are smoothed by a 9-month running mean filter.

in the negative phase. The intensification of the northern recirculation gyre at 37°N, 147°E is clearly seen in the positive phase (Fig. 3a). This result suggests that the first EOF mode captures both strength changes of the KE jet and its meridional shifts.

The time series of latitude and strength of the KE jet averaged between 140° and 165°E confirm their coherent variation (Fig. 4), and reveal a significant time lag between these variations. The latitude and strength of the KE jet exhibit similar decadal variability with PC1, with a typical amplitude of latitude and strength changes of 1° and 0.2 m s^{-1}. The lag correlation of the KE jet latitude and PC1 is the highest at zero lag ($r = 0.91$). On the other hand, the KE jet strength has the highest correlation with PC1 when PC1 leads by 9 months ($r = 0.89$). Consistently, the correlation between the latitude and the strength of the jet is the highest when the latitude variation leads by 9 months ($r = 0.85$). We can obtain similar results if the latitude and strength of the KE jet are averaged between 140° and 153°E. Simultaneous variations between the northward (southward) migration and intensification (weakening) of the KE jet have been reported by Qiu and Chen (2005, 2010) as the stable and unstable modes of the KE jet, but the time lag has not been reported previously. This time lag between latitude and strength of the KE jet suggests that meridional shifts of the KE jet are a key process in the decadal variability in the KE region, and will therefore be further examined in the next section.

4. Propagation signals

a. Relation to atmospheric fluctuations

In the previous section, we showed that the first EOF mode of low-frequency sea level variability in the KE region represents the meridional shift of the KE jet, followed by changes in strength after a 9-month lag. What is the cause of the meridional shift of the KE jet? Previous studies showed that atmospheric fluctuations in the central North Pacific induce westward propagating signals and cause the changes in the KE region several years later (e.g., Deser et al. 1999; Taguchi et al. 2007; Ceballos et al. 2009; Sasaki and Schneider 2011a). To identify the westward propagating signals, we first identify the lead–lag relation of the KE variability to atmospheric fluctuations using a SVD analysis.

When wintertime (November–March) Z_{1000} anomalies lead to SLAs in the KE region by 3 years, the squared covariance (SC) and squared covariance fraction (SCF) of the first SVD modes are the highest (Table 1). In addition, the correlation coefficient r between the two time series of the first SVD mode at the 3-yr lag is the second highest. This result indicates that sea level variability in the KE region responds to atmospheric fluctuations with a 3-yr lag (more accurately a 3.5-yr lag because wintertime Z_{1000} anomalies and annual mean SLAs are used), consistent with previous studies (e.g., Seager et al. 2001; Lysne and Deser 2002). Similar lead–lag relations can be obtained from the first SVD modes using the wintertime wind stress curl anomalies or

TABLE 1. Lag, squared covariance (SC), squared covariance fraction (SCF), and the correlation coefficient r between the time series of the first SVD modes between annual mean SLAs and wintertime Z_{1000}. Lag denotes how long Z_{1000} leads SLAs.

Lag (yr)	SC ($\times 10^{11}$)	SCF (%)	r
5	5.33	43.5	0.70
4	7.52	48.1	0.76
3	8.31	56.6	0.81
2	5.43	47.5	0.76
1	5.91	48.2	0.76
0	5.72	46.0	0.84

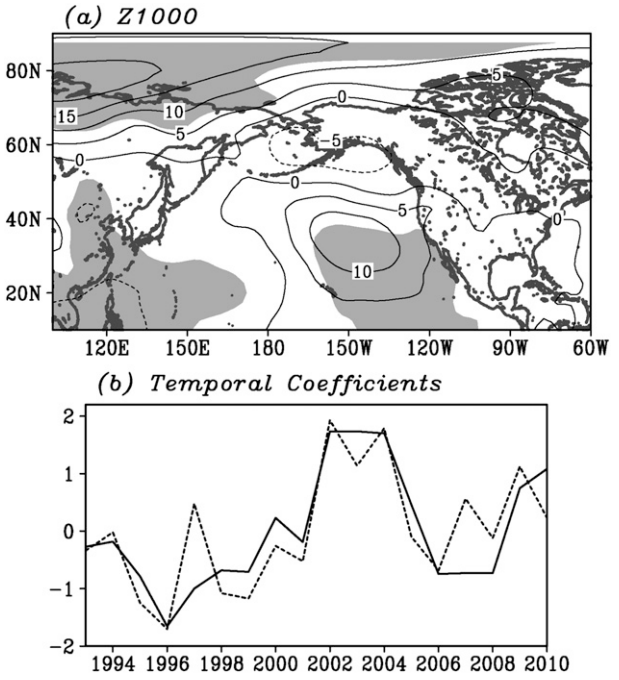

FIG. 5. The first SVD mode between annual mean SLAs from 1993 to 2010 and 3-yr leading Z_{1000} in winter (November–March) from 1990 to 2007. (a) Heterogeneous regression map for Z_{1000}: Contour interval 5 m; shading indicates regions where the corresponding correlations are significant at the 95% confidence level. (b) Normalized temporal coefficients for SLAs (solid line) and Z_{1000} (dashed line): time series for Z_{1000} are shifted backward by 3 yr.

annual mean Z_{1000} anomalies instead of the wintertime Z_{1000} anomalies over the North Pacific (not shown). Thus, we next examine in detail the first SVD mode at a 3-yr lag.

The time series of the first SVD mode for SLAs (solid line in Fig. 5b) exhibit prominent decadal variability that are highly correlated with annual mean SLA PC1 shown in Fig. 2b ($r = 0.96$). This means that the first SVD mode captures the same variability as the EOF mode of SLAs. The corresponding heterogeneous regression coefficients of Z_{1000} exhibit dipole anomalies over the North Pacific with positive Z_{1000} loading located over the eastern North Pacific at a latitude that roughly corresponds to the latitude of the KE jet, and weak negative Z_{1000} loading over Alaska (Fig. 5a). The homogeneous regression map of Z_{1000} also shows a similar dipole pattern with positive anomalies over the eastern North Pacific and weak negative anomalies over Alaska (not shown). This atmospheric dipole pattern resembles the North Pacific Oscillation (e.g., Walker and Bliss 1932; Linkin and Nigam 2008), although the expression over Alaska is weak. The positive Z_{1000} anomalies over the eastern North Pacific are accompanied by negative wind stress curl anomalies at the surface (not shown), which cause Ekman convergence in the upper ocean and likely induce positive SLAs. This suggests that the propagating signals originate in the eastern North Pacific. This point will be further investigated in the next subsection.

b. Westward propagation

In this subsection, we identify propagating signals and examine their features. The lagged regression coefficients of SLAs onto PC1 show westward propagation of positive SLAs from the eastern North Pacific to the upstream KE region (Fig. 6). Between -4 yr and -3 yr lag, the positive SLAs with a meridional extent of more than 1000 km and amplitude of about 3 cm emerge in the eastern North Pacific (Figs. 6a,b). This emergence of the positive SLAs in the eastern North Pacific is consistent with the positive Z_{1000} anomalies aloft (Fig. 5a). These positive SLAs propagate westward and reach in the upstream KE region after 3–4 years (Figs. 6c–e). During this propagation toward the upstream KE jet in the west, the meridional scale decreases and the amplitude increases. At 160°E the meridional scale is about 400 km, and the amplitude is about 10 cm (Fig. 6d). Farther upstream the meridional scale further sharpens to 200 km and the amplitude increases to more than 20 cm (Figs. 2a and 6e). Therefore, the change of the meridional scale of signals occurred during the westward propagation. This continuous narrowing of the meridional scale and increasing of the amplitude suggests that processes in the interior ocean, rather than in the western boundary, play an important role in changing the meridional scale and the amplitude. The role of processes around the western boundary, such as PV advection (e.g., Cessi et al. 1987; Taguchi et al. 2005), may be secondary.

A closer look at the propagation pathway west of the date line indicates that large SLAs closely followed the climatological jet position, especially from 140° to 170°E (left column in Fig. 7). At 3-yr lag the positive SLAs are

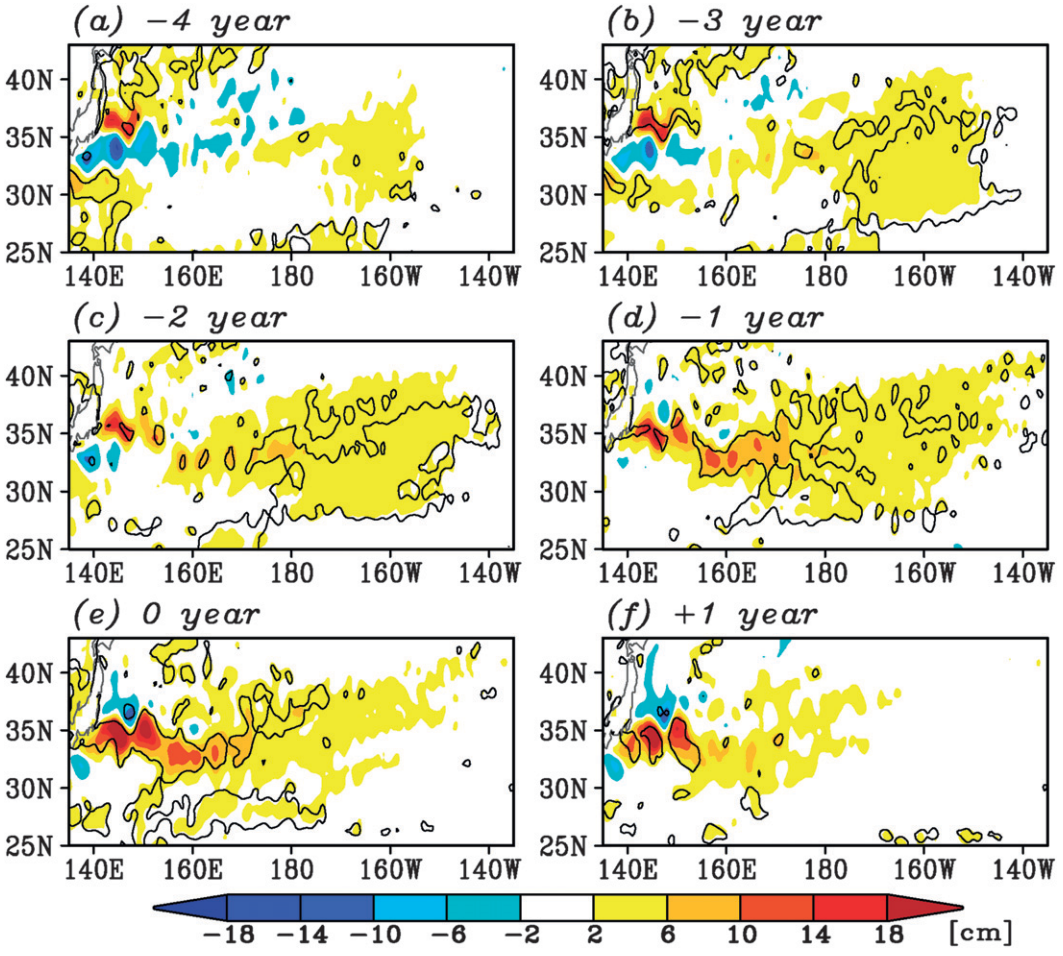

FIG. 6. Lag regressions of SLAs of the satellite observation onto PC1 for the lag year (a) −4, (b) −3, (c) −2, (d) −1, (e) 0, and (f) +1: negative lag means that PC1 lags SLAs. The SLA data are smoothed by a 9-month running mean filter. The contour indicates the regions where the corresponding correlations are significant at 95% confidence level.

located at 33°N east of 175°E (Fig. 7a). This latitude roughly corresponds to that of the climatological downstream KE jet. This signal propagates westward along 33°N (Fig. 7c), but the latitude of the signal shifts northward by about 2° around 155°E (Fig. 7e). This northward shift of the propagation pathway corresponds to the northward shift of the mean jet axis and the large sea level variability there (Fig. 1a). After the signal reaches the east coast of Japan, the large positive SLAs are located over the upstream KE jet axis, and the northern recirculation gyre at 37°N, 147°E starts to intensify (Fig. 7g). Thus, the KE jet acts as a waveguide of the propagation signals. This propagation pathway cannot be explained by the large-scale Rossby waves but is likely consistent with the thin-jet theory proposed by Sasaki and Schneider (2011a), who indicated that the meridional shifts of the jet propagate westward as Rossby waves trapped along a PV front associated with the jet. In contrast, east of the date line the intense KE jet disappears (Fig. 1b) and the SLAs are not likely constrained by the jet (Fig. 6b). This implies that there is a transient region of propagating signal properties around the date line.

c. *Propagation of the jet shift*

Here, we examine the relation between the SLAs and the shifts of the KE jet to understand this relation and to test the thin-jet theory. Figure 8 shows latitude anomalies of the KE jet. Consistent with Sasaki and Schneider (2011a), the latitude anomalies exhibit westward propagation tendency, albeit in a noisy fashion. The southward displacement of the jet starting from the date line in 1993–97 and 2004–07 and the northward displacement in the downstream region in 1998–2002 and after 2008 propagate westward.

Upon reaching the upstream KE region about 2–3 years later, the westward propagating signals account for dominant sea level variability in the KE region captured

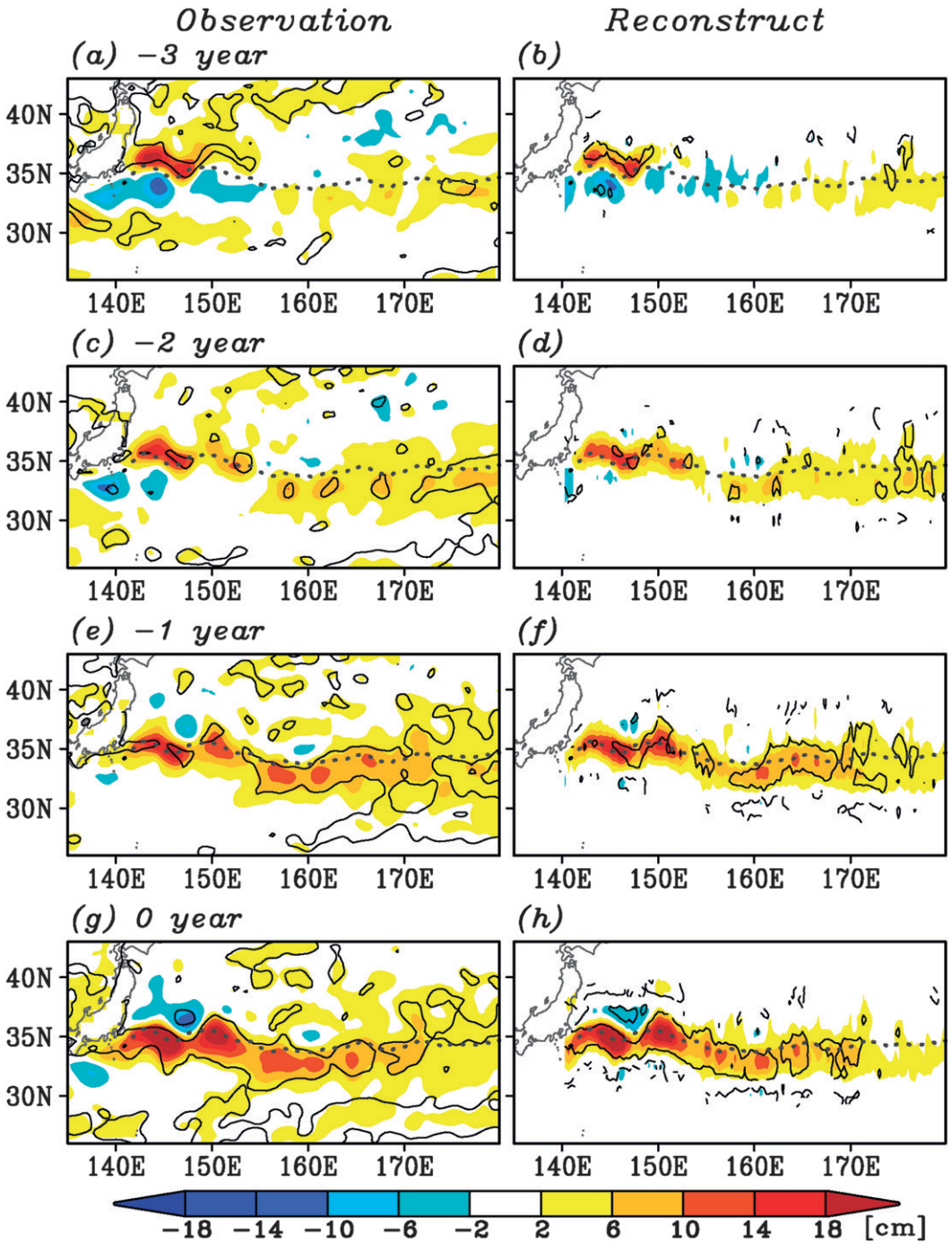

FIG. 7. Lag regressions of SLAs (left) of the satellite observation and (right) by the reconstruction (Eq. 1) onto PC1 for lag year (a),(b) −3; (c),(d) −2; (e),(f) −1; (g),(h) 0: negative lag means that PC1 lags SLAs. The SLA data are smoothed by a 9-month running mean filter. The black solid contour indicates the regions where the corresponding correlations are significant at the 95% confidence level. The gray dotted line denotes the climatological position of the KE jet. In the right column, statistical significance of the correlations is not drawn for the regions where absolute values of the corresponding regressions are less than 0.5 cm.

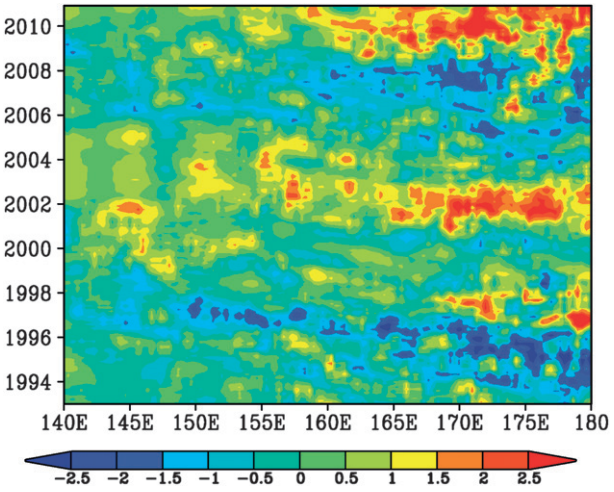

FIG. 8. Monthly mean latitude anomalies (deg) of the KE jet. The jet latitude data are smoothed by a 9-month running mean filter.

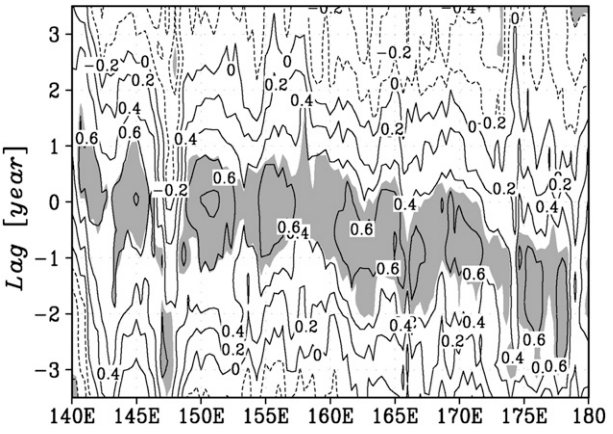

FIG. 9. Lag correlations of PC1 with the monthly-mean latitude of the KE jet: contour interval 0.1; shading indicates the regions where the correlations are significant at the 95% confidence level. Negative lag means that PC1 lags. Before calculating the correlations, a 9-month running mean filter is applied to the jet latitude data.

by the first EOF mode. The lead–lag correlations between PC1 and the latitude of the KE jet capture a westward propagation tendency from the date line to the upstream KE region (Fig. 9). The typical transit time of the propagation from 180° to 145°E is about 2 years, so the phase speed of the westward propagation is approximately 5.0 cm s^{-1}. In the thin-jet theory, the phase speed of disturbances of the PV front is given as the average of large-scale Rossby wave phase speeds north and south of the jet (Sasaki and Schneider 2011a). This observed phase speed of 5.0 cm s^{-1} is 1.6 times faster than the phase speed of the large-scale Rossby wave in the North Pacific basin (e.g., 3.1 cm s^{-1} at 35°N, Qiu 2003), possibly due to the longitude dependence of the phase speeds associated with stronger stratification in the western basin rather than in the eastern basin (Chelton and Schlax 1996; Chelton et al. 1998). Indeed, similar propagation speeds of Rossby waves (~4–5 cm s^{-1}) around the KE region has been reported by past studies (Aoki and Imawaki 1996; Wang et al. 1998).

The amplitude of the meridional displacement of the KE jet becomes gradually smaller from downstream to upstream (Fig. 8). Figure 10a shows the standard deviation of latitudinal fluctuations of the KE jet. The amplitude of the shift of the KE jet is about 140 km east of 170°E, and progressively decreases to the west by a factor of 2 to ~70 km in the upstream region. Similar changes of the amplitude of the shift are reported by Sasaki and Schneider (2011a) using an eddy-resolving model simulation. This change of the amplitude of the shift is likely similar to the change of the meridional scale of SLAs (Fig. 6) and will be further discussed below.

We now turn our attention to a quantitative relation of the jet displacement and sea level variability. Sasaki and Schneider (2011a) represented sea level variability caused by the shift of the jet in the thin-jet framework as follows:

$$\eta(x, y, t) = \overline{\eta}_L[x, y_0(x) + dy(x, t)], \tag{1}$$

where y_0 is the climatological latitude of the KE jet axis, dy is its monthly anomaly, and $\overline{\eta}_L$ is the climatological sea surface height in natural, along-jet and across-jet coordinates. The meridional gradient of the climatological sea surface height around the KE jet in natural coordinates is sharper than that in Cartesian coordinates (e.g., Waterman et al. 2011). The schematic sketch of this reconstruction is shown in Fig. 11. The frozen-in-time cross-jet sea level profile of Eq. (1) assumes that a PV difference between the northern and southern side of the jet is entirely determined by the upper layer thickness changes, which is approximately true for the decadal variations of the KE jet and is consistent with the thin-jet approximation. We perform the reconstruction of sea level variability west of the date line using this equation, where $\overline{\eta}_L$ is calculated at each longitude from the composite of the monthly sea surface height relative to the KE jet axis and dy is given by the observational values.

The regression coefficients of the reconstructed SLAs onto PC1 show large SLAs along the jet axis (right column in Fig. 7), which resemble the observed SLAs (left column in Fig. 7). Since the meridional displacement dy in Eq. (1) is given by the observed values, the

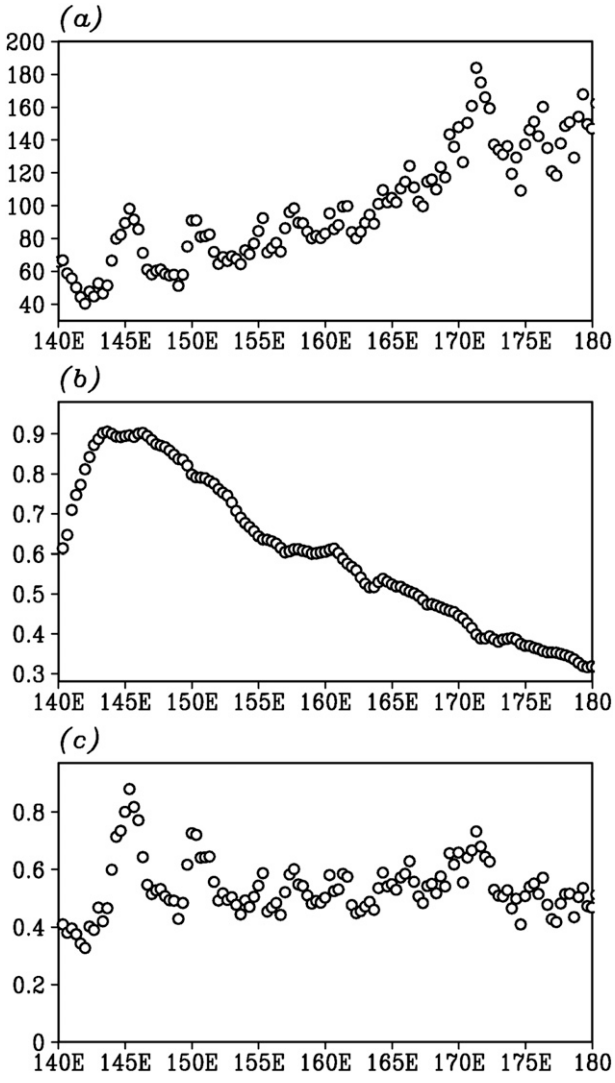

FIG. 10. (a) Standard deviation of the low-pass filtered monthly latitude of the KE jet (km); (b) mean across-jet sea level difference between 0.5° south of minus 0.5° north of the KE jet axis in natural coordinates (m); (c) product of the across-jet difference of sea level and the amplitude of the jet shift ($\times 10^5$ m^2).

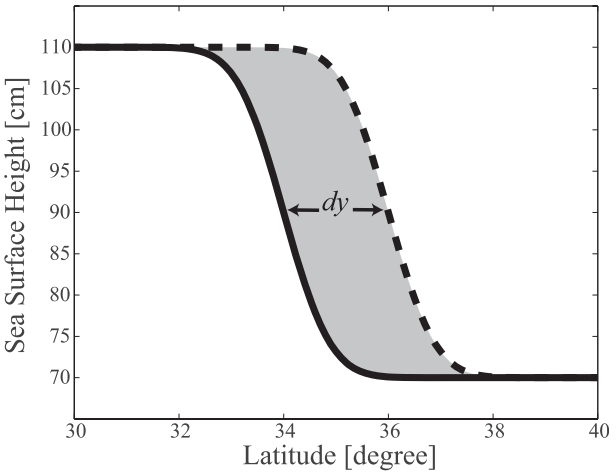

FIG. 11. Schematic diagram illustrating the reconstruction of sea level variability using Eq. (1). The solid line denotes the climatological sea surface height of the jet. Its northward displacement *dy*, shown by the dashed line, induces SLAs indicated by the gray shading.

matching of the zonal position of SLAs between the observation and the reconstruction is not surprising. It is still remarkable, however, that the meridional position, the amplitude and the meridional scale of the reconstructed SLAs match those of the observations. At 3-yr lag, the reconstruction reproduces the positive weak SLAs located around the jet axis east of 170°E with amplitude of about 3 cm (Figs. 7a,b). The positive SLAs around 33°–35°N east of 155°E in the reconstruction are quantitatively similar to those of the observations (Figs. 7c–f). Also, the reconstruction reproduces the northward shift of SLAs at 155°E from 33° to 35°N and large positive SLAs in the upstream KE region with amplitude of about 20 cm at 0-yr lag (Figs. 7g,h). These results indicate that the propagating signals of SLAs captured by the first EOF mode are dominated by the meridional shift of the KE jet. It is noteworthy that the region of large regression coefficients in the upstream KE region (west of 155°E) roughly correspond to the region of the poor reproduction of the SLA by a linear Rossby wave model shown by Qiu (2003) (see his Fig. 9). This indicates that the meridional migration of the upstream KE jet, which is well explained by the thin-jet model, cannot be explained by the linear long Rossby wave model.

The reconstruction using Eq. (1) also has implications for changes of the meridional scale and amplitude of SLAs in the course of the propagation shown in Fig. 6. The increase of the amplitude of SLAs from east to west results from the increase of the across-jet sea level difference in natural coordinates (Fig. 10b) because this difference determines amplitude of SLAs of the reconstruction by Eq. (1) (see Fig. 11). The across-jet sea level difference, which is proportional to the strength of the KE jet, is about 0.7–0.9 m (0.3–0.5 m) in the upstream (downstream) region. This decrease of the across-jet sea level difference to the east is related to the decrease of the KE jet transport. On the other hand, the change of meridional scale of SLAs is likely related to the change of amplitude of the jet displacement shown in Fig. 10a because the meridional extent of SLAs by reconstruction is simply proportional to the distance of the meridional jet displacement *dy* (Fig. 11). Hence, the characteristic changes of SLAs during propagation are likely related to the amplitude of the jet shift (Fig. 10a)

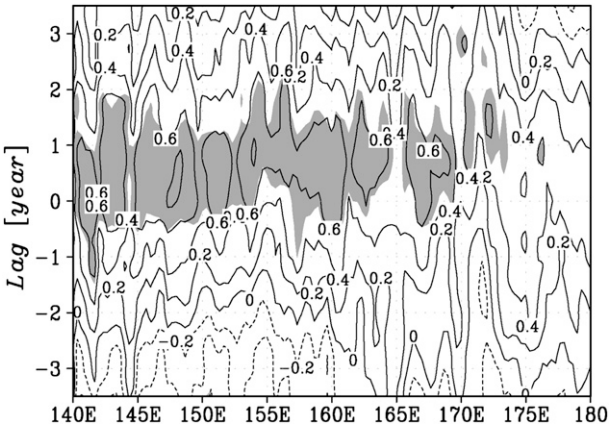

FIG. 12. Lag correlations of PC1 with the monthly mean jet absolute speed over the KE jet axis: contour interval 0.1; shading indicates the regions where the correlations are significant at the 95% confidence level. Negative lag means that PC1 lags. Before calculating the correlations, a 9-month running mean filter is applied to the jet speed data.

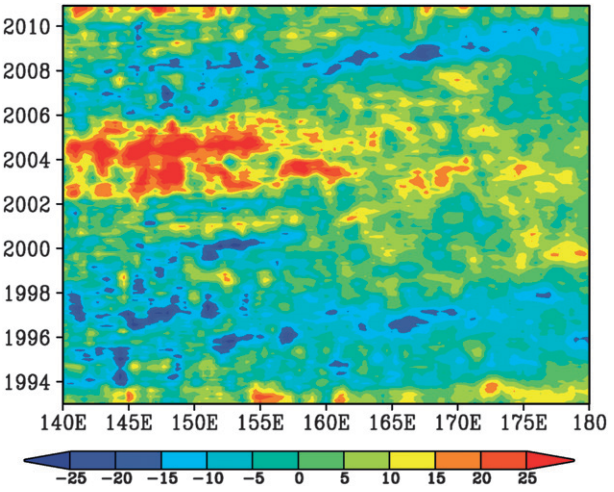

FIG. 13. Monthly mean jet absolute speed anomalies along the KE jet axis (cm s^{-1}): jet speed data are smoothed by a 9-month running mean filter.

and across-jet sea level difference of the KE jet (Fig. 10b).

From these results, one might expect the connection between amplitude of the jet shift and across-jet difference of sea level. It is worth noting that the product of the amplitude of the jet shift and the across-jet sea level difference is roughly constant at each longitude (Fig. 10c). Fluctuation of the product is less than 15% of its mean value except for the wavelike fluctuations west of 153°E, probably related to western boundary processes. Because the product of the amplitude of the jet shift and the across-jet sea level difference corresponds to volume (or quasigeostrophic PV) anomalies per unit length of longitude associated with the meridional displacement of the jet, as shown by the gray shading area in Fig. 11, these results suggest that the propagating signals conserve their quasigeostrophic PV anomalies at each longitude and therefore link the increase of SLAs and the decrease of their meridional scale in the course of the propagation (Fig. 6). This point will be further discussed in section 5.

d. Acceleration of the KE jet

After the westward propagating signals reach at the east coast of Japan, the northward (southward) shifts are followed by a strengthening (weakening) of the KE jet, as shown in the section 3. Here, we examine this lead–lag relation in further detail. The lead–lag correlation analysis of the strength of the KE jet onto PC1 reveals that the positive correlations in the upstream KE region reach their maximum after a few months lag (Fig. 12), consistent with the result shown in Fig. 4. This result also suggests that the acceleration of the KE jet propagates eastward from the western boundary to 170°E, in contrast to the westward propagation of the jet shift (Figs. 8 and 9). The eastward propagation speed of this signal is about 6 cm s^{-1}, comparable to the westward propagation of the meridional shifts of the KE jet.

The eastward propagating signals that often extend to 180° are also seen in the time–longitude plot of the absolute speed anomalies of the KE jet (Fig. 13). The weak current speed in the upstream region in 1993–2001 propagates eastward to the date line before 1998, while it disappears around 160°E after 1998. Similar eastward propagation of a negative velocity anomaly is found in the late-2000s. The upstream intensification of the KE jet in 2002–05 also propagates eastward. The amplitude of the surface velocity anomaly is about 0.2 m s^{-1} in the upstream region and decays weakly while propagating downstream. The values of the velocity anomalies correspond to one-fifth (one-third) of the mean surface current velocity in natural coordinates in the upstream (downstream) regions.

This eastward propagation cannot be explained by the thin-jet theory (Cushman-Roisin et al. 1993; Sasaki and Schneider 2011a). While the westward propagation of the jet-trapped Rossby waves is induced by the PV gradient effect as first-mode baroclinic Rossby waves, the eastward propagation may imply that the signals are advected by the current, such as the PV advection from the western boundary (e.g., Cessi et al. 1987). The eastward propagation with phase speed of a few centimeters per second suggests that this signal is higher-mode baroclinic Rossby waves (e.g., Liu 1999), although this hypothesis should be further confirmed by checking

a vertical structure of the signal. Taguchi et al. (2005) showed using an OGCM output that the inertial recirculation gyre of the KE jet accelerates due to the PV advection change after westward-propagating Rossby waves have arrived at the boundary. Furthermore, the PV advection from the western boundary plays an important role in the formation of the northern and southern recirculation gyres (Nakano et al. 2008). Hence, this eastward propagation supports the idea that the change of the PV advection induces the intensification of the KE jet through change of both northern and southern recirculation gyres. Consistently, the changes of the strength of the KE jet are associated with both the changes of the northern and southern recirculation gyres (Fig. 14), which exhibit an out-of-phase relation on decadal time scales. When the northern recirculation gyre changes lead the southern recirculation gyre changes by 6 months, the correlation between them is highest ($r = -0.65$). The sea level difference of the southern minus the northern recirculation gyres is highly correlated with the strength of the upstream KE jet ($r = 0.92$). Note that the strength changes of the KE jet are caused by not only the southern recirculation gyre changes but also the northern recirculation changes, which have received less attention in previous studies (e.g., Qiu and Chen 2005). Thus, the 9-month lag between the shift of the jet and its strength change documented in section 3 can be considered as a response time of the recirculation gyres to incoming jet-trapped Rossby waves along the KE jet.

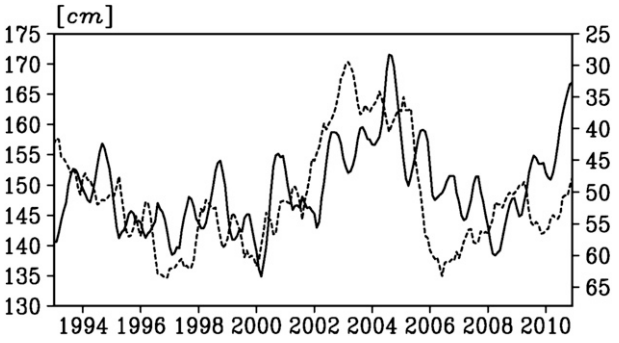

FIG. 14. Sea surface height south of the KE jet (solid line, left ordinate) and north of the KE jet (dashed line, right ordinate) averaged over 145°–153°E; the meridional extent of the northern (southern) recirculation gyre is from 0.5° to 2° north (south) of the jet axis. The two time series are smoothed by a 9-month running mean filter. The direction of the right ordinate is reversed.

5. Discussion

The conservation property for quasigeostrophic PV anomalies along the jet shown in Fig. 10c implies that we can empirically expand the thin-jet theory for a jet whose transport varies spatially. As for the thin-jet framework (Cushman-Roisin et al. 1993; Sasaki and Schneider 2011a), a 1.5-layer model is assumed, and the mean jet transport is prescribed by the difference of the sea surface height between the northern and southern edges of the jet $\Delta\eta$. The conservation of a quasigeostrophic PV anomaly is equivalent to the conservation of a volume anomaly per unit length of longitude along the jet as given by $\Delta\eta(x)\,dy(x,t)$ (see Fig. 11). Sasaki and Schneider (2011a) showed the westward propagation of meridional displacement of the KE jet using the thin-jet theory for the original form, that is, without including spatially varying $\Delta\eta(x)$. Thus, their numerical estimation of the jet displacement was an overestimation for the magnitude in the upstream KE region (see their Fig. 14), but taking account of the mean transport as a function of downstream distance we can overcome this shortcoming.

The above empirical relation indicates that, when the meridional displacement of the jet at the date line is known, then the meridional displacement of the upstream KE jet can be deduced, but another question should be discussed is how the jet displacement at the date line is determined. As shown before, the SLAs in the eastern North Pacific have a broad scale (Fig. 6) and are likely unconstrained by the KE jet. To quantitatively compare the broad-scale SLAs in the eastern North Pacific with the meridional shift of the downstream jet, we convert SLAs to the shift of the jet as follows:

$$\Delta Y \Delta\eta = \int \eta'\, dy, \tag{2}$$

where ΔY is a latitude anomaly of the jet, η' the SLAs, and $\Delta\eta$ is again the sea level difference between the south and north of the jet. The product of ΔY and $\Delta\eta$ provides an estimate of volume anomalies per unit length of longitude associated with the meridional displacement of the jet as shown in Fig. 10c. The rhs of Eq. (2) indicates a volume anomaly of the basin-scale SLAs in the eastern North Pacific, which is also proportional to their quasigeostrophic PV anomaly. Figure 15 shows the time series of the observed latitude anomaly of the downstream KE jet and the latitude anomaly (i.e., ΔY) estimated from SLAs in the eastern North Pacific (150°–170°W), where $\Delta\eta$ is set to 0.4 m (see Fig. 10b). When the time series of the jet latitude anomalies estimated from SLAs lead by 23 months, the two time series are highly positively correlated ($r = 0.67$, significant at 99% confidence level). This time lag suggests that the propagation speed from the eastern North Pacific to the downstream KE region is about 3.4 cm s^{-1}, consistent with the phase speed of the large-scale Rossby wave in the

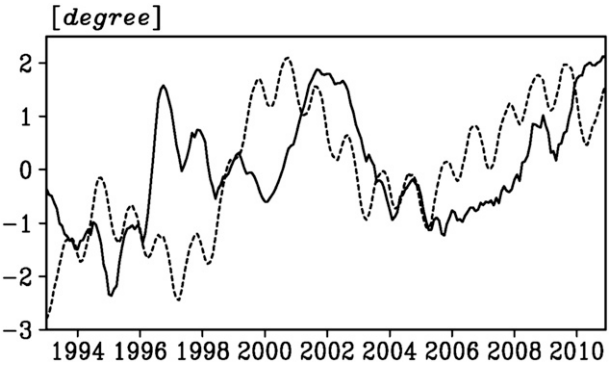

FIG. 15. Observed latitude anomalies of the KE jet averaged over 175°E–180° (solid line) and estimated from SLAs integrated over 30°–40°N and averaged over 150°–170°W (dashed line). The two time series are smoothed by a 9-month running mean filter.

North Pacific (e.g., 3.1 cm s^{-1} at 35°N, Qiu 2003). In addition, the estimated shift of the jet is comparable in amplitude to the shift of the downstream KE jet. Note that the estimated shift of the jet also has a significant correlation with PC1, when PC1 lags by 3 yr ($r = 0.75$). Thus, these results suggest that large-scale positive (negative) SLAs in the eastern North Pacific are converted to the northward (southward) shift of the downstream jet around the date line.

6. Conclusions

Interannual to decadal variability in the KE jet is examined using the satellite observations from 1993 to 2010. Dominant sea level variability in the KE region represents meridional shifts and strength changes of the KE jet on decadal time scales (Figs. 2 and 3), consistent with previous studies (Qiu and Chen 2005, 2010). However, a detailed analysis of the latitudes of the KE jet and its strength revealed that the northward (southward) displacement of the KE jet leads to the strengthening (weakening) of the jet by 9 months (Fig. 4). This result indicates that the latitude changes of the KE jet are a key process in the decadal variability in the KE region.

The meridional shifts of the KE jet lag atmospheric fluctuations in the eastern North Pacific by about 3 yr (Table 1 and Fig. 5). Consistent with the lagged relation, broad SLAs occur in the eastern North Pacific 3–4 years before the upstream KE jet shift, and propagate westward to the upstream KE region with that time lag (Figs. 6 and 7). It is worth emphasizing that, in the course of the propagation, the meridional scale of the SLAs gradually decreases, and their amplitude gradually increases at the same time. This westward propagation of SLAs is attributed to the westward propagation of the meridional shift of the jet axis with a speed of ~5 cm s^{-1} from the date line to the upstream KE region (Figs. 8 and 9). This propagation pathway and speed for westward propagating signals is consistent with the thin-jet theory (Sasaki and Schneider 2011a). The reconstruction of SLAs using Eq. (1) reveals the strong relation of westward propagating signals between SLAs and the shift of the jet (Fig. 7). This result also suggests that the meridional-scale change of the SLAs is related to the amplitude change of the meridional jet displacement (Fig. 10a). In addition, the gradual decrease of SLAs to the east is likely attributed to the decay of the jet (Fig. 10b). Interestingly, we found that this change of the strength of the jet is inversely proportional to the change of the amplitude of the jet shifts (Fig. 10c), suggesting conservation of quasigeostrophic PV anomalies. This conservation also suggests that broad-scale positive (negative) SLAs in the eastern North Pacific result in the northward (southward) shift of the downstream jet around the date line (Fig. 15). Thus, the spatial scale difference of the signals in the eastern North Pacific and the KE region is likely explained by the quasigeostrophic PV conservation and the interaction of the signals with the KE jet.

After the westward propagating signals reach at the east coast of Japan, the strength change of the KE jet emerges from the east coast of Japan and propagates eastward with a speed about 6 cm s^{-1} (Figs. 12 and 13). These strength changes of the KE jet are attributed to the coherent changes of the northern and southern recirculation gyres (Fig. 14). The eastward propagation of the strength change suggests the importance of advection by the current from the western boundary in response to the incoming signals from east along the KE jet axis. Hence, the time lag between the shift of the jet and its strength change can be considered as a response time of the recirculation gyres. Note that the advection from the western boundary likely plays an important role in SLAs in the Kuroshio–Oyashio confluence region north of the KE region, where previous studies showed that westward propagating signals do not enter (Qiu 2003; Nakano and Ishikawa 2010; Sugimoto and Hanawa 2011). In the present study, we have not investigated the detailed mechanism for the connection between the northward (southward) shift of the KE jet and the strengthening (weakening) of the northern and southern recirculation gyres because our thin-jet model does not include effects of the boundary processes. To explore the connection between the jet latitudes and the strength of the recirculation gyres, we need to examine PV changes at the subsurface where signals by the PV advection are prominent (Taguchi et al. 2005; Nakano et al. 2008). Although subsurface observations

are generally too sparse to resolve western boundary processes, it is desirable to investigate the subsurface process in the future. Understanding of this physical mechanism gives increased confidence in the relation between latitude and strength changes of the KE jet, which is still under debate whether they are coherent before the satellite altimeter era (e.g., Taguchi et al. 2007; Qiu and Chen 2010).

Acknowledgments. We thank two anonymous reviewers for comments that helped to improve the manuscript. This research was supported by the Grant-in-Aid for Scientific Research on Innovative Areas 22106008 and for Young Scientists (Start-up) 23840001, which are all funded by the Ministry of Education, Culture, Sports, Science, and Technology of Japan, the U.S. National Science Foundation Grants NSF OCE06047994 and NSF OCE0550233, and by the Office of Science (BER), U.S. Department of Energy, Grant DE-FG02-07ER64469 and Grant DE-SC0006766. We gratefully acknowledge additional support through the sponsorship of research at the International Pacific Research Center by the Japan Agency for Marine-Earth Science and Technology (JAMSTEC), by NASA through Grant NNX07AG53G, and by NOAA through Grant NA09OAR4320075.

REFERENCES

Anderson, D. L. T., and P. D. Killworth, 1979: Non-linear propagation of long Rossby waves. *Deep-Sea Res.,* **26,** 1033–1050.

Aoki, S., and S. Imawaki, 1996: Eddy activities of the surface layer in the western North Pacific detected by satellite altimeter and radiometer. *J. Oceanogr.,* **52,** 457–474.

Berloff, P., A. M. C. Hogg, and W. Dewar, 2007: The turbulent oscillator: A mechanism of low-frequency variability of the wind-driven ocean gyres. *J. Phys. Oceanogr.,* **37,** 2363–2386.

Bond, N. A., M. F. Cronin, and M. Garvert, 2010: Atmospheric sensitivity to SST near the Kuroshio Extension during the extratropical transition of Typhoon Tokage. *Mon. Wea. Rev.,* **138,** 2644–2663.

Bretherton, C. S., C. Smith, and J. M. Wallace, 1992: An intercomparison of methods for finding coupled patterns in climate data. *J. Climate,* **5,** 541–560.

Ceballos, L. I., E. Di Lorenzo, C. D. Hoyos, N. Schneider, and B. Taguchi, 2009: North Pacific gyre oscillation synchronizes climate fluctuations in the eastern and western boundary systems. *J. Climate,* **22,** 5163–5174.

Cessi, P., G. Ierley, and W. Young, 1987: A model of the inertial recirculation driven by potential vorticity anomalies. *J. Phys. Oceanogr.,* **17,** 1640–1652.

Chelton, D. B., and M. G. Schlax, 1996: Global observations of oceanic Rossby waves. *Science,* **272,** 234–238.

——, R. A. DeSzoeke, M. G. Schlax, K. El Naggar, and N. Siwertz, 1998: Geographical variability of the first baroclinic Rossby radius of deformation. *J. Phys. Oceanogr.,* **28,** 433–460.

Cushman-Roisin, B., L. Pratt, and E. Ralph, 1993: A general theory for equivalent barotropic thin jets. *J. Phys. Oceanogr.,* **23,** 91–103.

Deser, C., M. A. Alexander, and M. S. Timlin, 1999: Evidence for a wind-driven intensification of the Kuroshio Current Extension from the 1970s to the 1980s. *J. Climate,* **12,** 1697–1706.

Ducet, N., and P.-Y. Le Traon, 2001: A comparison of surface eddy kinetic energy and reynolds stresses in the Gulf Stream and the Kuroshio current systems from merged TOPEX/Poseidon and ERS-1/2 altimetric data. *J. Geophys. Res.,* **106** (C8), 16 603–16 622.

Frankignoul, C., N. Sennéchael, Y.-O. Kwon, and M. A. Alexander, 2011: Influence of the meridional shifts of the Kuroshio and the Oyashio Extensions on the atmospheric circulation. *J. Climate,* **24,** 762–777.

Gill, A. E., 1982: *Atmosphere-Ocean Dynamics.* Academic Press, 662 pp.

Itoh, S., I. Yasuda, H. Nishikawa, H. Sasaki, and Y. Sasai, 2009: Transport and environmental temperature variability of eggs and larvae of the Japanese anchovy (*Engraulis Japonicus*) and Japanese sardine (*Sardinops Melanostictus*) in the Western North Pacific estimated via numerical particle-tracking experiments. *Fish. Oceanogr.,* **18,** 118–133.

Jayne, S. R., and Coauthors, 2009: The Kuroshio Extension and its recirculation gyres. *Deep-Sea Res. I,* **56,** 2088–2099.

Joyce, T. M., and J. Dunworth-Baker, 2003: Long-term hydrographic variability in the northwest Pacific Ocean. *Geophys. Res. Lett.,* **30,** 1043, doi:10.1029/2002GL015225.

Kalnay, E., and Coauthors, 1996: The NCEP/NCAR 40-Year Reanalysis Project. *Bull. Amer. Meteor. Soc.,* **77,** 437–472.

Kaplan, D., and L. Glass, 1995: *Understanding Nonlinear Dynamics.* Springer-Verlag, 420 pp.

Kelly, K. A., R. J. Small, R. M. Samelson, B. Qiu, T. M. Joyce, Y.-O. Kwon, and M. F. Cronin, 2010: Western boundary currents and frontal air–sea interaction: Gulf Stream and Kuroshio Extension. *J. Climate,* **23,** 5644–5667.

Kwon, Y.-O., and C. Deser, 2007: North Pacific decadal variability in the Community Climate System Model version 2. *J. Climate,* **20,** 2416–2433.

——, M. A. Alexander, N. A. Bond, C. Frankignoul, H. Nakamura, B. Qiu, and L. A. Thompson, 2010: Role of the Gulf Stream and Kuroshio–Oyashio Systems in large-scale atmosphere–ocean interaction: A review. *J. Climate,* **23,** 3249–3281.

Latif, M., and T. P. Barnett, 1994: Causes of decadal climate variability over the North Pacific and North America. *Science,* **266,** 634–637.

Linkin, M. E., and S. Nigam, 2008: The North Pacific oscillation–west Pacific teleconnection pattern: Mature-phase structure and winter impacts. *J. Climate,* **21,** 1979–1997.

Liu, Z., 1999: Forced planetary wave response in a thermocline gyre. *J. Phys. Oceanogr.,* **29,** 1036–1055.

——, and L. Wu, 2004: Atmospheric response to North Pacific SST: The role of ocean–atmosphere coupling. *J. Climate,* **17,** 1859–1882.

Lysne, J., and C. Deser, 2002: Wind-driven thermocline variability in the Pacific: A model–data comparison. *J. Climate,* **15,** 829–845.

Maximenko, N., and Coauthors, 2009: Mean dynamic topography of the ocean derived from satellite and drifting buoy data using three different techniques. *J. Atmos. Oceanic Technol.,* **26,** 1910–1919.

Minobe, S., 2002: Interannual to interdecadal changes in the Bering Sea and concurrent 1998/99 changes over the North Pacific. *Prog. Oceanogr.,* **55,** 45–64.

Mizuno, K., and W. B. White, 1983: Annual and interannual variability in the Kuroshio Current System. *J. Phys. Oceanogr.,* **13,** 1847–1867.

Mochizuki, T., and Coauthors, 2010: Pacific decadal oscillation hindcasts relevant to near-term climate prediction. *Proc. Natl. Acad. Sci. USA,* **107,** 1833–1837.

Nakano, H., and I. Ishikawa, 2010: Meridional shift of the Kuroshio Extension induced by response of recirculation gyre to decadal wind variations. *Deep-Sea Res.,* **57,** 1111–1126.

——, H. Tsujino, and R. Furue, 2008: The Kuroshio Current System as a jet and twin ''relative'' recirculation gyres embedded in the sverdrup circulation. *Dyn. Atmos. Oceans,* **45,** 135–164.

Nishikawa, H., and I. Yasuda, 2008: Japanese sardine (*Sardinops Melanostictus*) mortality in relation to the winter mixed layer depth in the Kuroshio Extension region. *Fish. Oceanogr.,* **17,** 411–420.

——, and ——, 2011: Long-term variability of winter mixed layer depth and temperature along the Kuroshio jet in a high-resolution ocean general circulation model. *J. Oceanogr.,* **67,** 503–518.

Nitta, T., and S. Yamada, 1989: Recent warming of tropical sea-surface temperature and its relationship to the Northern Hemisphere circulation. *J. Meteor. Soc. Japan,* **67,** 375–383.

Nonaka, M., H. Nakamura, Y. Tanimoto, T. Kagimoto, and H. Sasaki, 2006: Decadal variability in the Kuroshio–Oyashio Extension simulated in an eddy-resolving OGCM. *J. Climate,* **19,** 1970–1989.

Oka, E., T. Suga, C. Sukigara, K. Toyama, K. Shimada, and J. Yoshida, 2011: ''Eddy resolving'' observation of the North Pacific Subtropical Mode Water. *J. Phys. Oceanogr.,* **41,** 666–681.

Pierini, S., H. A. Dijkstra, and A. Riccio, 2009: A nonlinear theory of the Kuroshio Extension bimodality. *J. Phys. Oceanogr.,* **39,** 2212–2229.

Qiu, B., 2003: Kuroshio Extension variability and forcing of the Pacific decadal oscillations: Responses and potential feedback. *J. Phys. Oceanogr.,* **33,** 2465–2482.

——, and S. Chen, 2005: Variability of the Kuroshio Extension jet, recirculation gyre, and mesoscale eddies on decadal time scales. *J. Phys. Oceanogr.,* **35,** 2090–2103.

——, and ——, 2010: Eddy–mean flow interaction in the decadally modulation Kuroshio Extension System. *Deep-Sea Res.,* **57,** 1098–1110.

——, and ——, 2011: Effect of decadal Kuroshio Extension jet and eddy variability on the modification of North Pacific Intermediate Water. *J. Phys. Oceanogr.,* **41,** 503–515.

Rio, M.-H., and F. Hernandez, 2004: A mean dynamic topography computed over the World Ocean from altimetry, in situ measurements, and a GEOID model. *J. Geophys. Res.,* **109,** C12032, doi:10.1029/2003JC002226.

Sasaki, Y. N., and N. Schneider, 2011a: Decadal shifts of the Kuroshio Extension jet: Application of thin-jet theory. *J. Phys. Oceanogr.,* **41,** 979–993.

——, and ——, 2011b: Interannual to decadal Gulf Stream variability in an eddy-resolving ocean model. *Ocean Modell.,* **39,** 209–219.

Schneider, N., and A. J. Miller, 2001: Predicting western North Pacific Ocean climate. *J. Climate,* **14,** 3997–4002.

——, ——, and D. W. Pierce, 2002: Anatomy of North Pacific decadal variability. *J. Climate,* **15,** 586–605.

Seager, R., Y. Kushnir, N. H. Naik, M. A. Cane, and J. Miller, 2001: Wind-driven shifts in the latitude of the Kuroshio–Oyashio Extension and generation of SST anomalies on decadal time scales. *J. Climate,* **14,** 4249–4265.

Sugimoto, S., and K. Hanawa, 2011: Roles of SST anomalies on the wintertime turbulent heat fluxes in the Kuroshio–Oyashio confluence region: Influences of warm eddies detached from the Kuroshio Extension. *J. Climate,* **24,** 6551–6561.

Sura, P., and S. T. Gille, 2010: Stochastic dynamics of sea surface height variability. *J. Phys. Oceanogr.,* **40,** 1582–1596.

Taguchi, B., S.-P. Xie, H. Mitsudera, and A. Kubokawa, 2005: Response of the Kuroshio Extension to Rossby waves associated with the 1970s climate regime shift in a high-resolution ocean model. *J. Climate,* **18,** 2979–2995.

——, ——, N. Schneider, M. Nonaka, H. Sasaki, and Y. Sasai, 2007: Decadal variability of the Kuroshio Extension: Observations and an eddy-resolving model hindcast. *J. Climate,* **20,** 2357–2377.

——, H. Nakamura, M. Nonaka, and S.-P. Xie, 2009: Influences of the Kuroshio/Oyashio Extensions on air–sea heat exchanges and storm-track activity as revealed in regional atmospheric model simulations for the 2003/04 cold season. *J. Climate,* **22,** 6536–6560.

Thompson, K. R., and E. Demirov, 2006: Skewness of sea level variability of the world's oceans. *J. Geophys. Res.,* **111,** C05005, doi:10.1029/2004JC002839.

Tokinaga, H., Y. Tanimoto, S.-P. Xie, T. Sampe, H. Tomita, and H. Ichikawa, 2009: Ocean frontal effects on the vertical development of clouds over the western North Pacific: In situ and satellite observations. *J. Climate,* **22,** 4241–4260.

Trenberth, K. E., 1990: Recent observed interdecadal climate changes in the Northern Hemisphere. *Bull. Amer. Meteor. Soc.,* **71,** 988–993.

Walker, G. T., and E. M. Bliss, 1932: World Weather V. *Mem. Roy. Meteor. Soc.,* **4,** 53–84.

Wang, L., C. J. Koblinsky, and S. Howden, 1998: Annual and interannual sea level variability in the region of the Kuroshio Extension from TOPEX/Poseidon and *Geosat* altimetry. *J. Phys. Oceanogr.,* **28,** 692–711.

Waterman, S., N. G. Hogg, and S. R. Jayne, 2011: Eddy–mean flow interaction in the Kuroshio Extension region. *J. Phys. Oceanogr.,* **41,** 1182–1208.

Yatsu, A., T. Watanabe, M. Ishida, H. Sugisaki, and L. D. Jacobson, 2005: Environmental effects on recruitment and productivity of Japanese sardine *Sardinops Melanostictus* and chub mackerel *Scomber Japonicus* with recommendations for management. *Fish. Oceanogr.,* **14,** 263–278.